

Dry Printing and Additive Nanomanufacturing of Flexible Hybrid Electronics and Sensors

Zabihollah Ahmadi, Seungjong Lee, Aarsh Patel, Raymond R. Unocic, Nima Shamsaei, and Masoud Mahjouri-Samani*

The growing demand for flexible and wearable hybrid electronics has triggered the need for advanced manufacturing techniques with versatile printing capabilities. Complex ink formulations, use of surfactants/contaminants, limited source materials, and the need for high-temperature heat treatments for sintering are major issues facing the current inkjet and aerosol printing methods. Here, the nanomanufacturing of flexible hybrid electronics (FHE) by dry printing silver and indium tin oxide on flexible substrates using a novel laser-based additive nanomanufacturing process is reported. The electrical resistance of the printed lines is tailored during the print process by tuning the geometry and structure of the printed samples. Different FHE designs are fabricated and tested to check the performance of the devices. Mechanical reliability tests including cycling, bending, and stretching confirm the expected performance of the printed samples under different strain levels. This transformative liquid-free process allows the on-demand formation and in situ laser crystallization of nanoparticles for printing pure materials for future flexible and wearable electronics and sensors.

complicated, time and energy-consuming, relatively expensive, and produce a large amount of waste materials (washing–cleaning–disposal requirements).^[8] Thus, much effort has been put toward inventing new techniques for direct printing and additive manufacturing of electronics on desired flexible and rigid substrates,^[9–18] such as polyimide and polyethylene terephthalate (PET).^[19–21] Different fabrication strategies have been proposed for additive nanomanufacturing of electronics.^[22–27] The most common direct-write technologies in the field of printed electronics are inkjet printing (IJP) and aerosol jet printing (AJP).^[6,28–32] These technologies allow the precise deposition of liquids containing functional materials. Recently, Patil et al. printed silver (Ag) nanowires (resistance < 50 Ω sq⁻¹) on flexible substrates via inkjet printing.^[33] Gilshtein et al. demonstrated inkjet-printed indium

tin oxide (ITO) patterns with a resistivity of $3.1 \times 10^{-3} \Omega$ cm on soda-lime glass.^[34] Chen et al. showed aerosol jet printing of Ag with a sheet resistance of $1.13 \times 10^{-2} \Omega$ m⁻² on cellulose fiber paper substrate.^[31] However, the current ink formulations used in IJP and AJP processes make device fabrication more complicated because they require toxic solvents and additives that limit the substrate's compatibility and hinder the device's performance.^[35,36] Also, nozzle clogging in IJP is a common and extremely complex phenomenon.^[37] Furthermore, to guarantee a high conductivity of the printed structures, AJP usually requires a high sintering temperature (e.g., ≈ 280 °C) and a long sintering time (e.g., 12 h on a glass substrate). This limits the AJP to only a few types of substrates.^[31] As a result, a new direct printing and patterning method is needed to overcome the challenges. Moreover, the new printing and patterning methods also need to be capable of printing structures with good reliability under repeated mechanical bending and unbending processes.

Motivated by these challenges, here, we demonstrated a novel additive nanomanufacturing (ANM) technique recently developed in our lab for manufacturing FHEs and sensors by printing conductive Ag and ITO on different flexible platforms such as polyimide and PET substrates. Conductive Ag is typically used to print electronic tracks, electrodes and antennas.^[38,39] Transparent conductors such as ITO are utilized in the printing of components such as flexible strain sensors, solar cells, and organic light-emitting diodes (OLEDs).^[40–43]

1. Introduction


The research and development efforts on flexible hybrid electronics (FHEs) have been rising rapidly due to its wide range of applications in healthcare, consumer products, automotive, aerospace, and energy industries.^[1–7] The conventional lithography-based processes for manufacturing electronics are often

Z. Ahmadi, A. Patel, M. Mahjouri-Samani
Electrical and Computer Engineering Department
Auburn University
Auburn, AL 36849, USA
E-mail: mzm0185@auburn.edu

S. Lee, N. Shamsaei
Department of Mechanical Engineering
Auburn University
Auburn, AL 36849, USA

S. Lee, N. Shamsaei, M. Mahjouri-Samani
National Center for Additive Manufacturing Excellence (NCAME)
Auburn University
Auburn, AL 36849, USA

R. R. Unocic
Center for Nanophase Materials Sciences
Oak Ridge National Laboratory
Oak Ridge, TN 37831, USA

 The ORCID identification number(s) for the author(s) of this article can be found under <https://doi.org/10.1002/admi.202102569>.

DOI: 10.1002/admi.202102569

The main principle of our ANM printer is the in situ formation of pure and dry nanoparticles produced by condensation of laser-plasma plume in atmospheric Ar pressure, which is then guided through a nozzle onto a substrate that is sintered in real-time, forming the desired patterns. The mechanical reliability of ANM-printed samples has been shown by investigating the resistance change of the samples via bending and cycling tests. FHEs and sensors such as near-field communication (NFC) tag antenna, ITO-based strain sensor and lighting circuits were fabricated on polyimide and PET substrates to demonstrate their performances in this printing approach. This novel ANM and device manufacturing method is a promising technology for future manufacturing of the FHEs and sensors directly from dry and pure nanoparticles generated and sintered in on-demand and in real-time.

2. Experimental Section

Figure 1 shows the schematic illustration of the ANM printer consisting of a microchamber, a rotating target, a nozzle, and a gas flow feeder system. A Coherent COMPex excimer laser (KrF, pulse duration 25 ns) beam was divided into two paths; one for laser ablation (LA) and the other for laser

sintering (LS) processes in the ANM system. These beams were focused onto the surface of targets and substrates via UV convex lenses. Depending on the type of the materials and substrates, LA and LS beams' energy were adjusted to achieve the formation and sintering of desired nanoparticles. Focused LA beam hits the rotating targets, which will result in the formation of plasma plume that interacts with background Ar gas resulting in condensations and formation of nanoparticles on-demand. These nanoparticles were then directed toward the substrate through a nozzle with different diameters ranging from 100 to 300 μm using a carrier gas. The LS beam with suitable energy sinters and crystallizes the arrived nanoparticles onto the substrate's surface in real-time. As more nanoparticles arrive, the deposition increases and forms a continuous film.

The substrates were placed on an XY positioning stage and moved according to the preprogrammed path. The distance between the apex of the nozzle and the substrate was kept constant at ≈ 0.5 mm. Commercially available Ag and ITO targets with 99.99% purity were used for the ablation and formation of nanoparticles. The diameter of the nozzles used in ANM printer determined the feature size of the printed lines. The thickness of the printed lines was controlled by printing speed as well as the number of layer-by-layer printed paths.

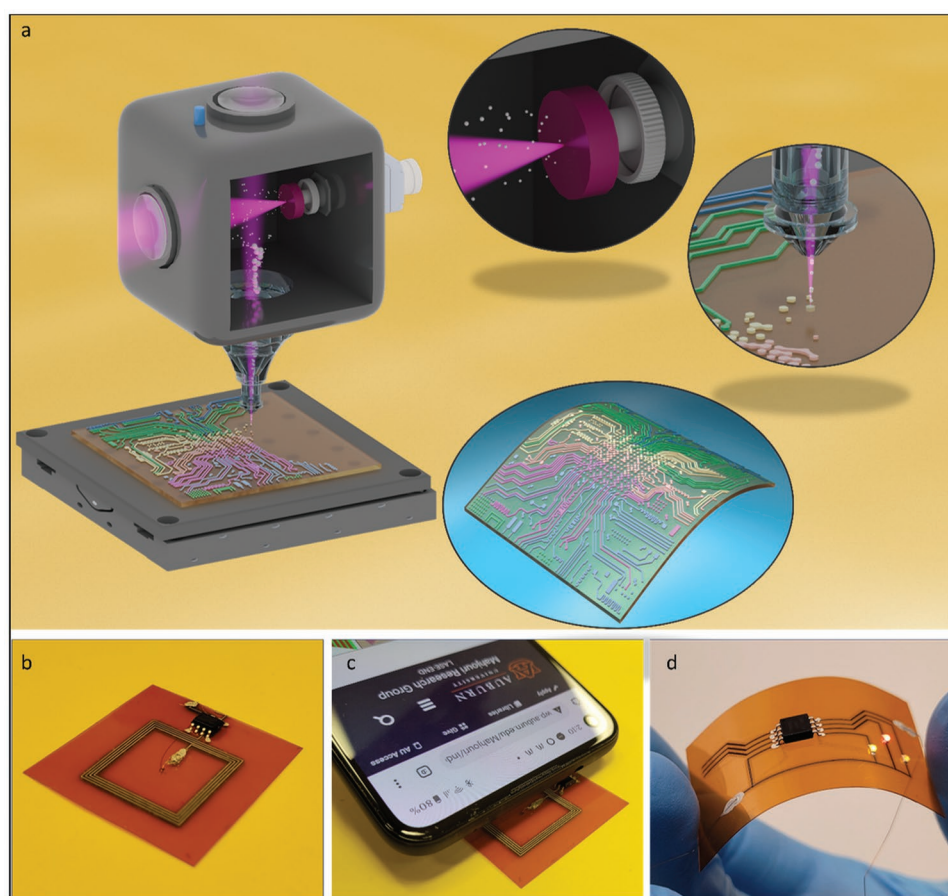


Figure 1. a) Schematic illustration of ANM process for dry printing Ag and ITO on flexible substrates. b,c) A 2×2 cm² printed Ag NFC tag antenna (four loops with a total length of ≈ 32 cm and $\approx 1.38 \Omega$ cm resistance) connected to a self-power M24LR04E IC enabling communication with a phone device. d) Printed FHEs circuit on the polyimide substrate.

It should be noted that since only an excimer laser for the ablation and sintering process was used, the repetition rate was always the same for ablation and sintering processes. Typically, lasers with shorter wavelengths (higher photon energy) and shorter pulse widths (high peak power) are suitable for the efficient ablation of a wide range of solid targets. Also, depending on the type of materials and substrates involved in the process, various sintering energies should be employed. Moreover, the shallow absorption depth of UV laser used here allowed to slightly sinter the generated nanoparticles without damaging the underlying substrates.

Figure 1b shows an example of a $2 \times 2 \text{ cm}^2$ printed Ag NFC tag antenna (four loops with a total length of $\approx 32 \text{ cm}$ and $\approx 1.38 \Omega \text{ cm}$ resistance) printed on a polyimide substrate. The mounted M24LR04E IC was programmed to launch the group's website. As shown in Figure 1c, the group website pops up on display by holding the cellphone in the proximity ($\approx 1 \text{ cm}$) of the printed NFC tag. Figure 1d demonstrates the printed FHEs circuit on the polyimide substrate via ANM process.

3. Results and Discussions

3.1. Nanoparticles Generation and Sintering

To confirm the nanoparticle formation and analyze their size distribution, we performed scanning electron microscopy (SEM) and scanning transmission electron microscopy (STEM) measurements on the as-generated nanoparticles. While the LS beam was blocked, we collected laser-ablated Ag and ITO nanoparticles (ablation energy (AE) = 2 J cm^{-2} , gas flow rate (GFR) = 2.8 SLPM, sintering/crystallization energy (S/CE) = blocked, repetition rate (RR) = 10 Hz). The SEM images of the unsintered and laser-sintered nanoparticles are shown in Figure 2a,d. Figure 2b,e shows the bright-field (BF) STEM images of the captured Ag and ITO nanoparticle, which were directly deposited onto the TEM grids for measurements. According to the STEM images, the size of the generated nanoparticles was in the range of 3–10 nm diameters. The unsintered nanoparticles form a fluffy structure that is loosely attached to the substrate. When

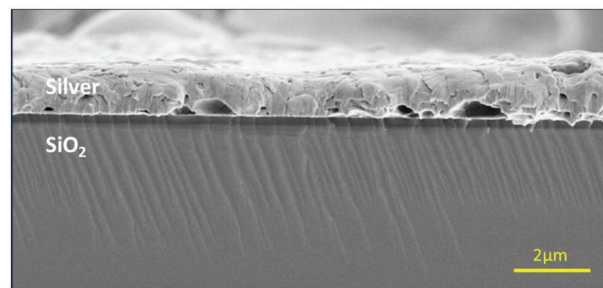


Figure 3. Cross-sectional image of printed and sintered silver nanoparticles on SiO_2 substrate via ANM process.

these nanoparticles were laser sintered during the process, they fused together to form a solid line. Figure 2c,f shows the sintered Ag and ITO nanoparticles. The sintering energy was 0.08 and 0.13 J cm^{-2} for Ag and ITO, respectively. Figure 3 shows a cross-sectional SEM image of the printed Ag line confirming the sintering of the ablated nanoparticles on SiO_2 substrate.

SEM images in Figure 4 show the morphological and electrical resistance evolution of the sintered Ag nanoparticles at different sintering laser energies. By increasing the crystallization energy while other parameters (AE = 2 J cm^{-2} , RR = 40 Hz, GFR = 2.8 SLPM, laser beam overlap = 93%, deposition time in each point = 20 ms, number of printed path = 6, and nozzle diameter size = $300 \mu\text{m}$) are kept constant, the nanoparticles start to fuse together. The highest porosity was seen at the lower sintering energy ($\approx 0.03 \text{ J cm}^{-2}$), and the lowest porosity was achieved at the higher laser sintering energy ($\approx 0.11 \text{ J cm}^{-2}$), as shown in Figure 4a,i, respectively. It should be noted that the laser energies below the abovementioned lowest threshold did not impact the particles, and energies above the higher threshold resulted in reablation of the deposited particles. Moreover, the electrical resistivity of the printed lines decreased as the sintering laser energy increased (shown in the upper right corner of the figures). As it has shown in Figure 4a–i, 40 and $7 \Omega \text{ cm}$ resistance were measured for lowest and highest sintering laser energies, respectively.

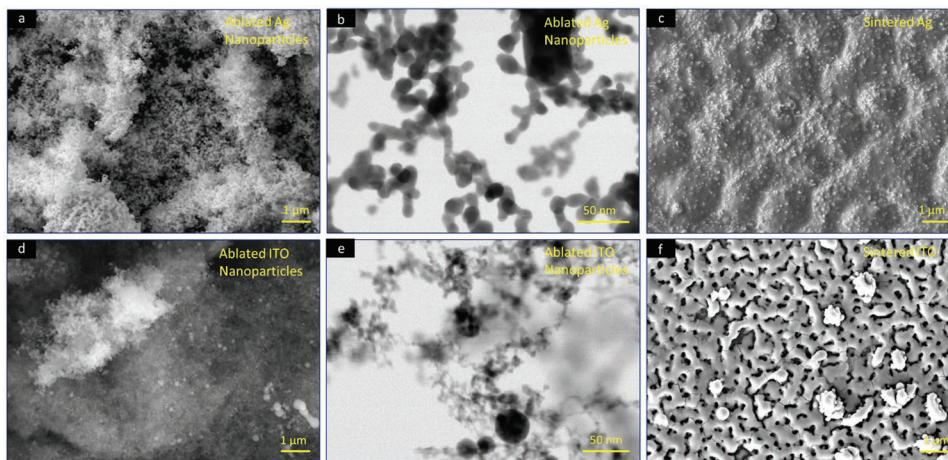


Figure 2. a,d) SEM images of laser-ablated Ag and ITO nanoparticles, respectively. b,e) BF-STEM images of laser-ablated Ag and ITO nanoparticles, respectively. SEM images of laser-sintered c) Ag and f) ITO.

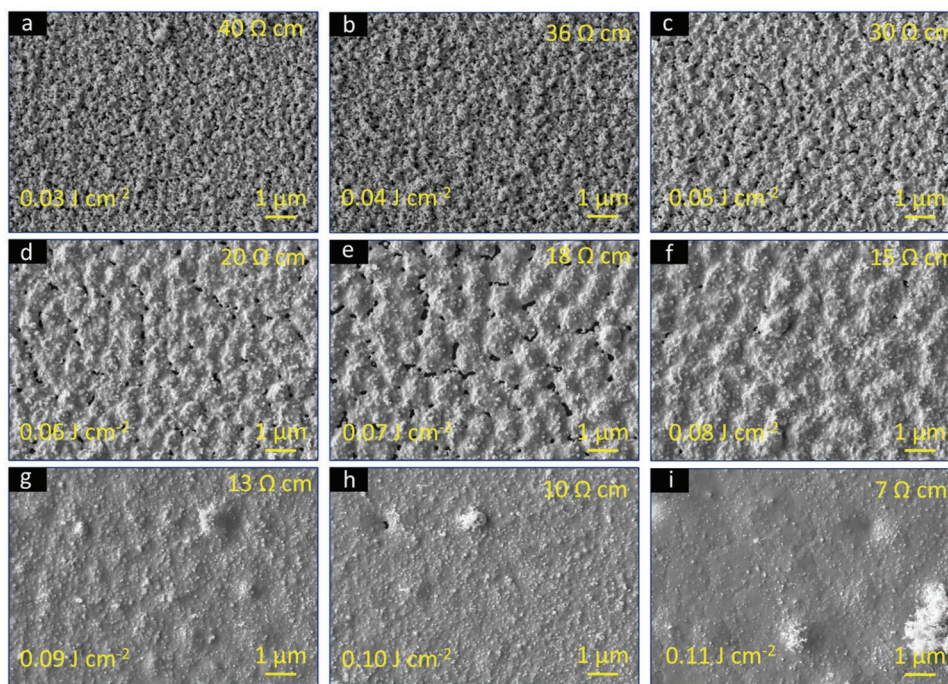


Figure 4. a–i) SEM images of morphological evolution of the printed Ag lines with different sintering laser energies as indicated on the bottom left corner of each figure. By increasing the sintering/crystallization energies, the porosity and resistance (shown upper right corner of each figure) of the printed lines decreased accordingly.

3.2. Factors Determining Electrical Properties of the ANM-Printed Lines

For the given process parameters ($AE = 2 \text{ J cm}^{-2}$, $S/CE = 0.09$ (Ag) and 0.39 (ITO) J cm^{-2} , $GFR = 2.8$ SLPM, laser beam overlap = 93%, deposition time in each point = 20 ms and nozzle diameter size = 300 μm), the thickness variation of the printed Ag and ITO lines on the polyimide substrates was analyzed at four different laser repetition rates (i.e., 10, 20, 30, and 40 Hz), as shown in **Figure 5**. In the case of Ag (Figure 5a), at 10 Hz repetition rate, the thickness increased from ≈ 1 to $\approx 60 \mu\text{m}$ when the number of printed paths increased from 1 to 20. Also, while the repetition rate increased (e.g., 40 Hz), the thickness of printed Ag layers increased in each path compared

to a lower repetition rate (e.g., 10 Hz). This could be attributed to the fact that the ablation rate and hence the number of in situ generated and sintered nanoparticles increase at higher repetition rates. The influence of gas flow rate (GFR), repetition rate (RR), and laser sintering/crystallization energy (S/CE) on thickness and resistance of printed TiO_2 and ITO is comprehensively discussed in our previous work,^[2] where we showed that the thickness of the ANM-printed TiO_2 is directly proportional to the number of printed paths and repetition rate.

Here, we have also performed a systematic study to investigate the influence of repetition rates and the number of printed paths on the printing speed and electrical conductivity of printed Ag lines on polyimide substrates. Similar information for ITO lines are reported in our previous study.^[2] **Figure 6a–d** represents

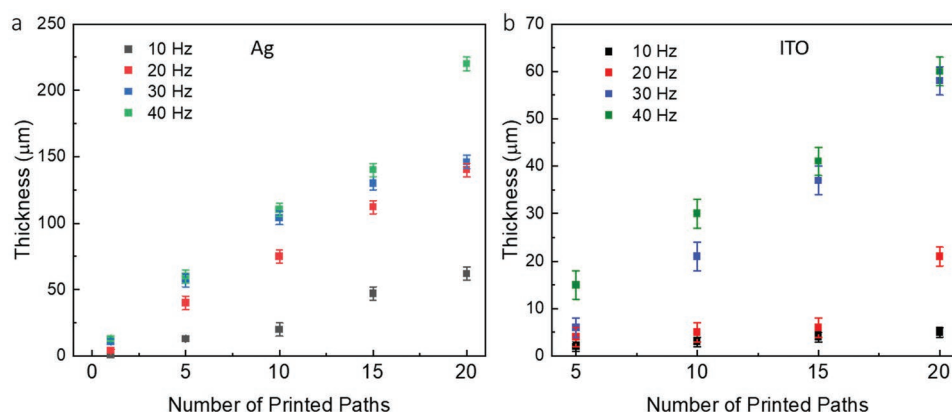


Figure 5. The thickness of sintered a) Ag and b) ITO as a function of the number of the printed paths at 4 different repetition rates 10, 20, 30, and 40 Hz.

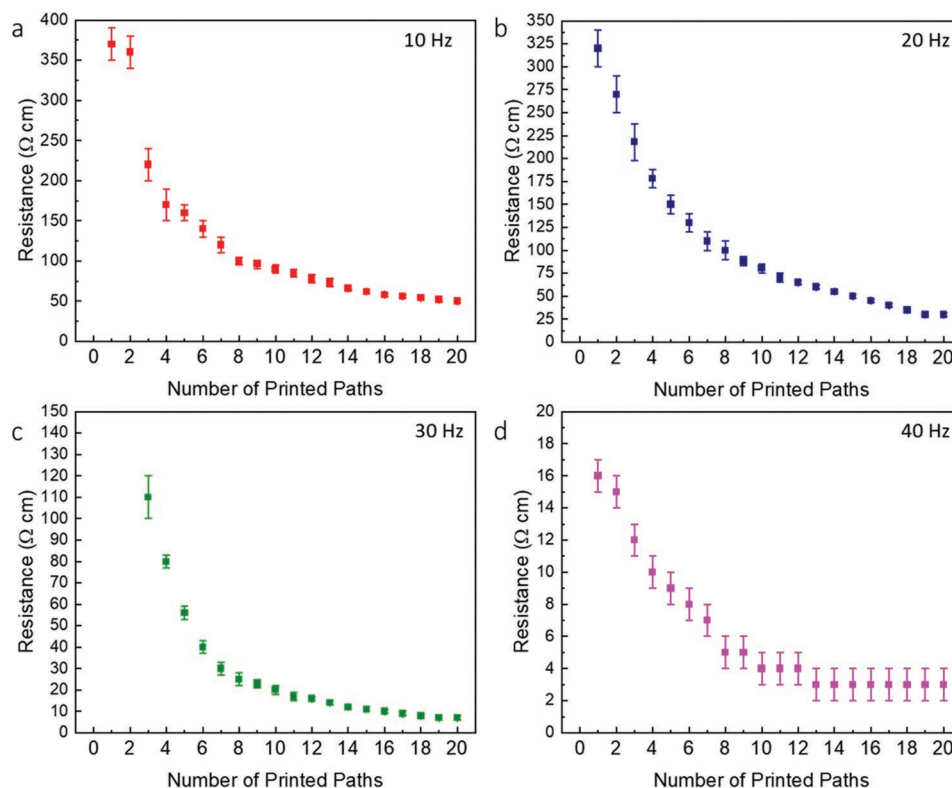


Figure 6. Resistance of ANM-printed Ag lines as a function of the number of printed paths for four different repetition rates, including a) 10 Hz, b) 20 Hz, c) 30 Hz, and d) 40 Hz.

the real-time resistance monitoring of 1 cm long printed Ag lines on polyimide substrates at different repetition rates ranging from 10 to 40 Hz while other parameters were kept constant ($AE = 2 \text{ J cm}^{-2}$, $S/CE = 0.1 \text{ J cm}^{-2}$, $GFR = 2.8 \text{ SLPM}$, laser beam overlap = 93%, deposition time in each point = 20 ms, and nozzle diameter size = $300 \mu\text{m}$). As shown in Figure 6, the electrical resistance of the printed lines decreased by increasing the number of printed paths and hence increasing the thickness of the printed lines, while the length and width of the printed resistor line remained unchanged. Also, increasing the repetition rate from 10 to 40 Hz increased the line thickness and hence reduced the resistance down to $\approx 16 \Omega \text{ cm}$ with just one path of printing. It can be seen from Figure 6a,b that using 40 Hz repetition rate and one-time printing path, the resistance reaches $\approx 16 \Omega \text{ cm}$, while for achieving the same resistance at 10 Hz repetition rate, the number of printed paths should be around 30 times. The Ag resistance could be tuned from $0.02 \Omega \text{ cm}$ to $\approx 200 \text{ K}\Omega \text{ cm}$ by adjusting the abovementioned process parameters. As a result, the ANM-printed lines and materials could be potentially used to realize fully printed

FHEs. The print resolution of the ANM was tested down to $100 \mu\text{m}$ using common commercial printing nozzles. It should be noted that printing thinner lines (e.g., $< 100 \mu\text{m}$) may be possible using smaller diameter nozzles since our ANM technique uses nanoparticles with an average size of 3–10 nm. Also, the spot size of the sintering laser can be reduced down to a few microns with suitable optics. Therefore, a combination of a nozzle with a smaller hole and the sintering laser with a smaller spot size can facilitate smaller line widths.

3.3. Reliability Testing of the ANM-Printed Ag Lines on Flexible Substrates

To test the reliability of the printed lines, we printed a set of Ag lines on $127 \mu\text{m}$ thick polyimide with the experimental parameters shown in Table 1. The reliability of these ANM-printed lines was investigated under the static and cyclic bending studies. Consequently, mechanical strain such as bending, cycling, and stretching may change the electrical performance

Table 1. Experimental parameters used for printing samples of Figure 7.

Figure 7	AE [J cm^{-2}]	S/CE [J cm^{-2}]	GFR [SLPM]	RR [Hz]	Number of printed path	Deposition time in each point [ms]	Nozzle diameter size [μm]
b	2	0.08	2.8	10	30–40	20	300
c	2	0.08	2.8	10	30–40	20	300
d	2	0.08	2.8	40	1–7	20	300

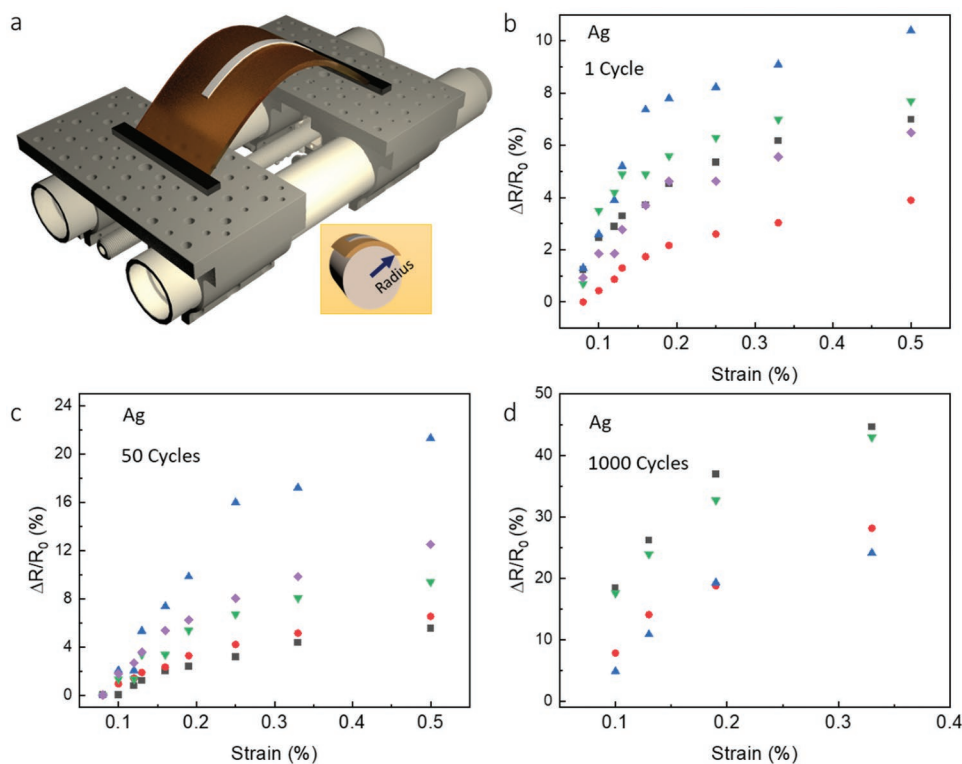


Figure 7. a) Schematic illustration of bending/cycling testing setup. Bending results of the ANM-printed Ag line for b) 1 cycle and c) 50 cycles. (Initial resistance: red, 10.8 Ω cm; purple, 13.6 Ω cm; black, 22.5 Ω cm; green, 25 Ω cm; blue, 22.4 Ω cm). d) Bending results of the ANM-printed Ag lines after 1000 cycles; (Initial resistance: red, 6.4 Ω cm; black, 20 Ω cm; green, 6.5 Ω cm; blue, 8.3 Ω cm).

of the printed lines. Thus, we performed in situ measurements to measure the changes in the resistance of the printed lines under different bending radii and compressive stresses. **Figure 7a** shows the schematic of the bending/cycling test setup. For instance, we tested different bending radii ranging from 77 to 16 mm equivalent to 0.08–0.5% strain. **Figure 7b–d** shows the variations in the electrical resistance of printed Ag lines as a function of different strains at three different numbers of cycles. The resistance change ($\Delta R/R_0$) and the strain on the device were calculated using the equations:

$$\frac{\Delta R}{R_0} (\%) = \frac{R_s - R_0}{R_0} \times 100 \quad (1)$$

$$\text{Strain} (\%) = \frac{t_{\text{substrate}}}{2R_{\text{bend}}} \times 100 \quad (2)$$

where R_0 , R_s , $t_{\text{substrate}}$, R_{bend} are initial resistance, under-stress resistance, substrate thickness, and bending radius, respectively.^[44,45] In the case of Ag, the resistance increased as it was bent for just one cycle, but the values of the resistance did not change drastically from the initial resistance values (e.g., $R_0 = 10.4 \Omega$ cm to $R_s = 11.5 \Omega$ cm at the maximum strain of 0.5%). As it is shown in **Figure 7b–d**, the resistance increased more at higher bending strains (lower bending radius). As shown in **Figure 7b**, the largest change in resistance was for conditions where the initial resistance was 22.4 Ω cm, and the

final resistance was 25.5 Ω cm at 0.5% strain. Also, the smallest change in the resistance seen in **Figure 7b** was for resistance changing from an initial resistance value of 10.8 Ω cm to a final resistance of 10.9 Ω cm at 0.08% strain.

The results from the 50 cycling tests are demonstrated in **Figure 7c**. According to the results, the resistance increased only slightly. The mean average of the overall change in resistance was 1.97 Ω cm. Thus, these Ag samples could tolerate a large strain with a slight increase in their electrical resistance. The results for 1000 cycles for different strains are presented in **Figure 7d**. Also, we observed that during the first 50 000 cycles, the resistance increased for a 10 Ω cm Ag line up to $\approx 20 \Omega$ cm (i.e., 100%), then the resistance started to increase continuously to more than $\approx 38 \Omega$ cm at 1 000 000 cycles. Relaxation time for this sample was around ≈ 1 h, and the final measured resistance was $\approx 27 \Omega$ cm. Low resistance deviation in bending radius beyond 40 mm (0.19% strain) and after numerous folding/unfolding cycles demonstrates the reliability of ANM printing process for manufacturing flexible electronics and sensors. Similar to the IJP and AJP, the increase in electrical resistance could be attributed to the formation of cracks in deposited materials. When the substrate is stretched, the high flexibility of the substrate and the less stretchable Ag causes crack formation, which ultimately causes the change of the resistance. Higher bending and stress accelerated the dislocation and crack formation in the sintered materials.

4. Functionality Demonstration

4.1. Printing Strain and Temperature Sensors

ITO is a transparent conducting layer that has been used in numerous applications. Although ITO has a low sheet resistance and excellent transparency, printed ITO lines on flexible substrates are usually micro/nanocrystalline structures with grain boundaries and pores, which might form micro/nano-cracks under tensile strains. These changes in properties can be exploited for strain sensors, touchscreens, and motion detectors applications.^[41]

We used a servohydraulic fatigue testing machine for displacement-controlled stretching tests, as shown in **Figure 8a**. ITO lines were printed onto the PET substrates ($55 \times 5 \times 0.175 \text{ mm}^3$) using process parameters reported previously.^[2] Stretching tests

for the printed ITO lines on PET were performed for different stretch levels. The amount of stretch was controlled with a precision of 0.18% to 0.9% displacement. All of the stretched samples were subjected to 100 cycles. For instance, **Figure 8b** shows the change in the resistance when subjected to 0.18–0.9% displacement for a printed ITO sample with initial resistance of $\approx 1.18 \text{ K}\Omega \text{ cm}$. For the case of 0.18% displacement, the resistance change was less than 5%, while for 0.36% displacement, it is about 16%. For the case of 0.54% to 0.72% displacement, the resistance change was around $\approx 50\%$. Applying 0.9% displacement resulted in a gradual resistance change of up to $\approx 400\%$. Above 0.9% displacement, permanent substrate plastic deformation was observed, resulting in resistance overload. The cycling frequency was kept at 1 Hz for all the samples.

The bending experiment was also used to demonstrate how the ITO resistance changes at different bending radii, as

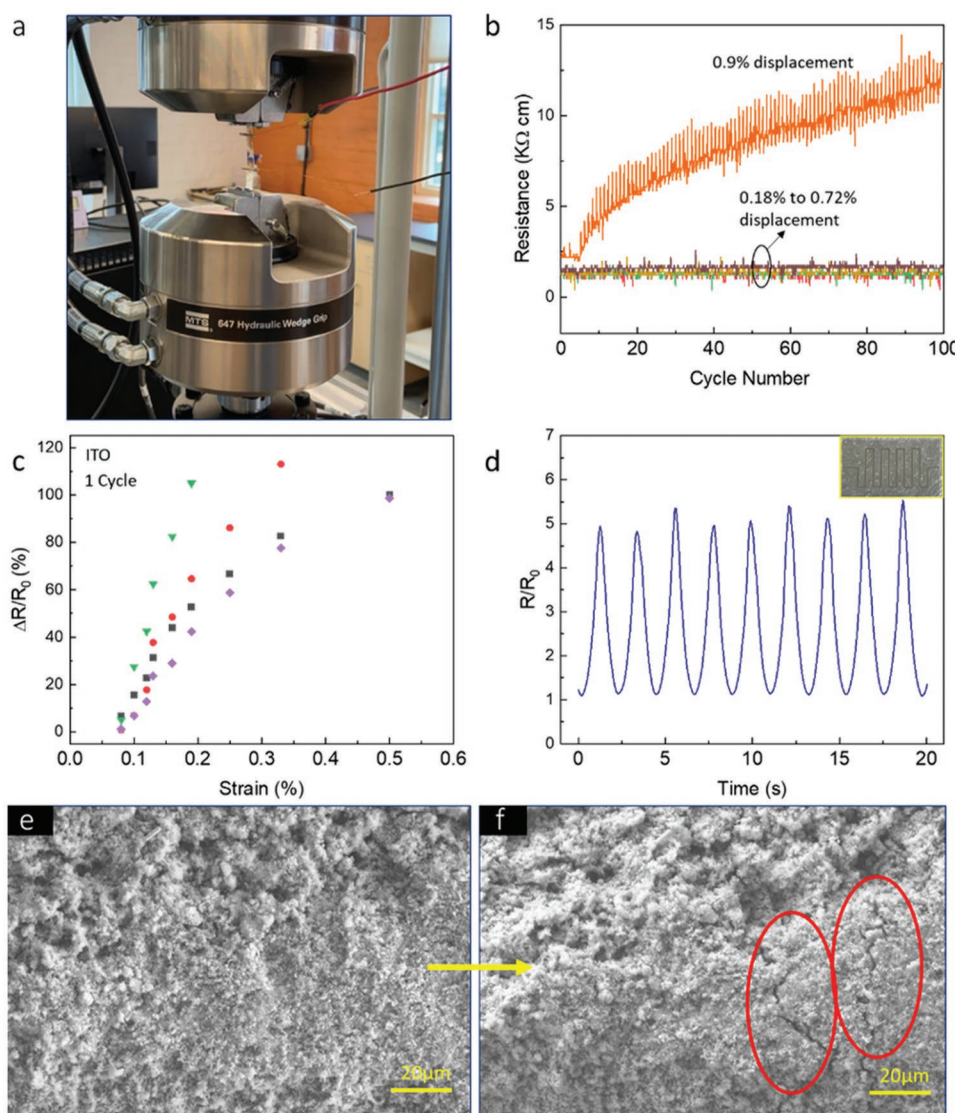


Figure 8. a) Digital image of fatigue setup used for stretching tests. b) Change of resistances in ANM-printed ITO strain sensor during 100 cycles at different strain levels. c) ITO bending results printed by ANM system for 1 cycle; Initial resistance: purple, $420 \Omega \text{ cm}$; black, $550 \Omega \text{ cm}$; red, $1300 \Omega \text{ cm}$; green, $1600 \Omega \text{ cm}$. d) The graph of normalized resistance variance at 0.19% strain during 9 cycles at 20 s (inset is the optical image of the ITO strain sensor). SEM images of the ITO surface e) before and f) after stretching showing signs of crack formation (red ellipse).

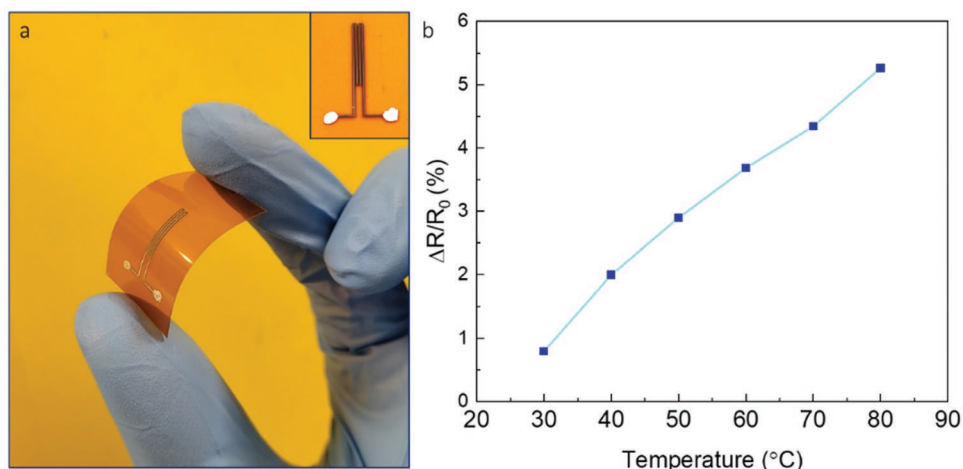


Figure 9. a) Optical image of a bent temperature sensor. The inset image shows the top-view picture of the temperature sensor. b) Relative resistance changes at temperatures ranging from 30 to 80 °C.

shown in Figure 8c. The initial resistance of printed samples was between 420 to 1600 Ω cm. Figure 8d shows the normalized resistance variance of strain sensor during 20 s at 0.19% strain and 9 cycles. The inset image in Figure 8d shows the printed ITO strain sensor on PET substrate. Furthermore, Figure 8e,f shows the SEM images of an ITO line before and after stretching. As it is shown in Figure 8f, under 0.9% displacement applied strain, small cracks appeared in the line that dramatically increased its resistance. Increased strain levels increase the crack density and widen the spacing between them, and hence the resistance increases. Adversely, when the cracks close, the resistance decreases.

4.2. Ag Temperature Sensor

Ag meander-shaped ribbon (300 μ m width and 1.5 cm length) was ANM-printed as a temperature sensor, as shown in Figure 9a. The sample was placed onto a hotplate to measure the sensor response, and the temperature measurement range

was performed from 30 to 80 °C with 10 °C temperature increment and 5 min wait time at each temperature. Figure 9b presents the percentage of resistance change at different temperatures. The sensor temperature coefficient resistance was extracted to be about $8.77 \times 10^{-4} \text{ } ^\circ\text{C}^{-1}$ which is comparable with other Ag-based temperature sensors.^[46]

4.3. Printing Flexible Hybrid Electronics (FHEs)

We designed and constructed several device prototypes to demonstrate the flexibility and applicability of our ANM process in printing FHEs on a polyimide substrate (Figure 10). As it is shown in Figure 10a, on the first step, conductive Ag tracks of the designed circuit were printed on polyimide substrates. Surface mount devices (SMD) and packaged electronic components (ICs and light-emitting diodes (LEDs)) were mounted on the predefined positions (Figure 10b). IC's pins and LEDs pads were connected to the ANM-printed circuit using a fast-drying Ag paint. The AT-Tiny 85 was programmed by configuring

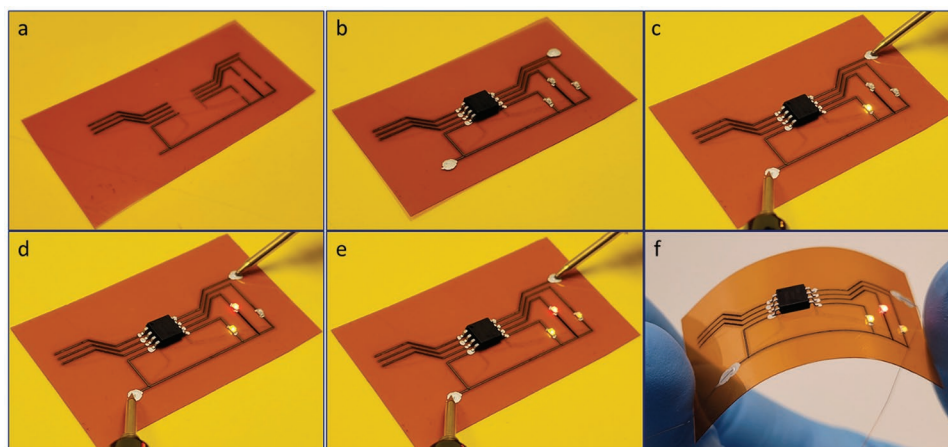


Figure 10. a) Conductive electronics circuit and pattern of Ag printed by ANM process on polyimide substrate. b) Mounted SMD IC and LEDs on the circuit. c–e) Sequential turning on LEDs programmed by IC while 5V is applied. f) Circuit working under bending pressure.

an Arduino-Uno as an In-System Programming (ISP) using the Arduino IDE software. The program initialized the designated pins (0, 1, and 2) on the AT-Tiny 85 board (running at 8 MHz) as output pins for LED's and ran an infinite loop for sequentially powering the LED's with set delays. By applying 5 V voltage to the circuit, as shown in Figure 10c–e, the LED's were turning on in sequential order. Figure 10f shows the circuit operating while it is bent and under strain.

5. Conclusion

In summary, we demonstrated the dry printing and additive nanomanufacturing of FHEs and sensors on flexible polyimide and PET substrates. In situ laser-generated nanoparticles inside a microchamber were used as the building blocks for printing conductive and functional lines and patterns. A real-time laser sintering process was used to sinter the nanoparticles onto the substrate as they exit the nozzle at room temperature and atmospheric pressure. Thin Ag and ITO patterns with resistances down to 0.02 and 100 Ω cm, respectively, were achieved by controlling the number of printed paths and repetition rates while using optimum sintering laser energy. Mechanical reliability tests including cycling (0.08% to 0.5% strain) and stretching (0.18% to 0.9% displacement) were performed on the additively manufactured Ag and ITO lines on 127 μ m thick polyimide and 200 μ m thick PET substrates. The results showed that all the Ag lines are still conductive at the highest testes strain, even after 1 000 000 cycles. Also, \approx 5% to \approx 400% change in resistance of ITO-printed lines under 0.18% to 0.9% displacement was observed. Conductive NFC antenna tag, strain sensor, temperate sensor, and FHEs were printed on polyimide and PET substrates, and their reliable performance was confirmed. The dry nature, printing flexibility, purity, mechanical reliability, and device performance characteristics demonstrate the potential use of the developed system as an alternative and transformative approach for future printed flexible electronics and sensors.

6. Methods and Characterizations

The \approx 12.5 Ω cm temperature sensor was printed using ANM printer and the following parameters. The ablation energy, sintering/crystallization energy, gas flow rate, and repetition rate were set at 2 J cm^{-2} , 0.07 J cm^{-2} , 2.8 SLPM, 20 Hz, respectively. 15 times printed path was employed with 93% laser beam overlap, 20 ms delay on each spot, and 300 μ m nozzle diameter size.

FHE circuit printed while ablation energy, sintering/crystallization energy, gas flow rate, and repetition rate were 2 J cm^{-2} , 0.09 J cm^{-2} , 2.8 SLPM, 20 Hz, respectively. Laser beam overlap, delay on each spot, nozzle diameter size, and the number of the printed paths set to 93%, 20 ms, 300 μ m, and 20 times, respectively.

SEM images were obtained using Zeiss Crossbeam 550 microscope. The voltage and current were 5 KV and 2 nA, respectively.

STEM imaging was performed using a Cs corrected JEOL NeoARM operating at 80 kV. Nanoparticles were directly

deposited onto the TEM grid by holding the TEM grids under the printer nozzle for a few seconds. Samples were then studied under TEM without further sample preparations. This collection method ensured the purity and cleanliness of the collected nanoparticles.

KEYENCE VHX-6000 series microscope was used to measure the thickness of ANM-printed samples.

Tabletop MTS Landmark servohydraulic test system with a load capacity of 25 kN was used to conduct displacement-controlled stretching tests.

Acknowledgements

This work was partially supported by the U.S. National Science Foundation (NSF) under grant No. 1923363. STEM characterization was conducted at the Center for Nanophase Materials Sciences (CNMS), which is a DOE Office of Science User Facility. Also, thanks to Mrs. Riley Laurendine for helping with the electrical measurements.

Conflict of Interest

The authors declare no conflict of interest.

Author Contributions

Z.A. designed and performed the experimental setup, synthesis and processing experiments, materials characterization, data analysis, and manuscript writing. S.L. participated in the SEM imaging, mechanical tests, and data analysis. A.P. participated in reliability tests and analysis experiments. R.R.U. participated in STEM imaging and analysis experiments. N.S. participated in experimental design, data analysis, and discussions. M.M.S. led the project, participated in experimental design, data acquisition and analysis, discussions, and manuscript preparation. All of the authors participated in manuscript preparation and revision processes.

Data Availability Statement

The data that support the findings of this study are available from the corresponding author upon reasonable request.

Keywords

additive nanomanufacturing, dry printing, flexible hybrid electronics, laser sintering, printed electronics

Received: December 28, 2021
Revised: January 29, 2022
Published online: February 24, 2022

- [1] Z. Ahmadi, S. Lee, R. R. Unocic, N. Shamsaei, M. Mahjouri-Samani, in *Laser 3D Manufacturing VIII*, International Society for Optics and Photonics, Bellingham, Washington, USA **2021**, 116770U.
- [2] Z. Ahmadi, S. Lee, R. R. Unocic, N. Shamsaei, M. Mahjouri-Samani, *Adv. Mater. Technol.* **2021**, 6, 2001260.
- [3] Y. Khan, A. Thielens, S. Muin, J. Ting, C. Baumbauer, A. C. Arias, *Adv. Mater.* **2019**, 32, 1905279.

- [4] L. Liu, Z. Shen, X. Zhang, H. Ma, J. *Colloid Interface Sci.* **2021**, *582*, 12.
- [5] R. D. Rodriguez, S. Shchadenko, G. Murastov, A. Lipovka, M. Fatkullin, I. Petrov, T. H. Tran, A. Khalelov, M. Saqib, N. E. Villa, V. Bogoslovskiy, Y. Wang, C. G. Hu, A. Zinovyev, W. Sheng, J. J. Chen, I. Amin, E. Sheremet, *Adv. Funct. Mater.* **2021**, *31*, 2008818.
- [6] G. Tarabella, D. Vurro, S. Lai, P. D'Angelo, L. Ascari, S. Iannotta, *Flexible Printed Electron.* **2020**, *5*, 014005.
- [7] Z. Zhou, H. Zhang, J. Liu, W. Huang, *Giant* **2021**, *6*, 100051.
- [8] A. H. Espera, J. R. C. Dizon, Q. Chen, R. C. Advincola, *Prog. Addit. Manuf.* **2019**, *4*, 245.
- [9] C. Zhao, P. J. Shah, L. J. Bissell, *Nanoscale* **2019**, *11*, 16187.
- [10] M. S. Alam, Q. Zhan, C. Zhao, *Nano Lett.* **2020**, *20*, 5057.
- [11] E. Castillo-Orozco, R. Kumar, A. Kar, *J. Laser Appl.* **2019**, *31*, 022015.
- [12] S. Wang, Y. Yu, D. Ma, D. Bridges, G. Feng, A. Hu, *J. Laser Appl.* **2017**, *29*, 022203.
- [13] A. Hu, R. Li, D. Bridges, W. Zhou, S. Bai, D. Ma, P. Peng, *J. Laser Appl.* **2016**, *28*, 022602.
- [14] P. Pathak, E. Castillo-Orozco, R. Kumar, A. Kar, H. J. Cho, *J. Laser Appl.* **2021**, *33*, 012034.
- [15] A. Zolfaghari, T. Chen, A. Y. Yi, *Int. J. Extreme Manuf.* **2019**, *1*, 012005.
- [16] F. Fang, N. Zhang, D. Guo, K. Ehmann, B. Cheung, K. Liu, K. Yamamura, *Int. J. Extreme Manuf.* **2019**, *1*, 012001.
- [17] Q. Ge, Z. Li, Z. Wang, K. Kowsari, W. Zhang, X. He, J. Zhou, N. X. Fang, *Int. J. Extreme Manuf.* **2020**, *2*, 022004.
- [18] Z. Lao, R. Sun, D. Jin, Z. Ren, C. Xin, Y. Zhang, S. Jiang, Y. Zhang, L. Zhang, *Int. J. Extreme Manuf.* **2021**, *3*, 025001.
- [19] A. Gumyusenge, X. Luo, Z. Ke, D. T. Tran, J. Mei, *ACS Mater. Lett.* **2019**, *1*, 154.
- [20] F. Yin, J. Yang, H. Peng, W. Yuan, *J. Mater. Chem. C* **2018**, *6*, 6840.
- [21] V. Zardetto, T. M. Brown, A. Reale, A. Di Carlo, *J. Polym. Sci., Part B: Polym. Phys.* **2011**, *49*, 638.
- [22] T. Santaniello, P. Milani, *Front. Nanosci.* **2020**, *15*, 313.
- [23] G. Shin, B. Jeon, Y.-L. Park, *J. Micromech. Microeng.* **2020**, *30*, 034001.
- [24] S. Kee, P. Zhang, J. Travas-Sejdic, *Polym. Chem.* **2020**, *11*, 4530.
- [25] K. N. Al-Milaji, Q. Huang, Z. Li, T. N. Ng, H. Zhao, *ACS Appl. Electron. Mater.* **2020**, *2*, 3289.
- [26] K.-S. Kwon, M. K. Rahman, T. H. Phung, S. Hoath, S. Jeong, J. S. Kim, *Flexible Printed Electron.* **2020**, *5*, 043003.
- [27] C. Zhao, *Laser additive manufacturing at*, inOSA Advanced Photonics Congress (AP), (IPR, NP, NOMA, Networks, PVLED, PSC, SPPCom, SOF), **2020**.
- [28] M. Singh, H. M. Haverinen, P. Dhagat, G. E. Jabbour, *Inkjet Printing Processes Appl. Adv. Mater.* **2010**, *22*, 673.
- [29] N. C. Raut, K. Al-Shamery, *J. Mater. Chem. C* **2018**, : 29. 1618.
- [30] A. Sajedi-Moghaddam, E. Rahmanian, N. Naseri, *ACS Appl. Mater. Interfaces* **2020**, *12*, 34487.
- [31] Y.-D. Chen, V. Nagarajan, D. W. Rosen, W. Yu, S. Y. Huang, *J. Manuf. Processes* **2020**, *58*, 55.
- [32] N. Čatić, L. Wells, K. Al Nahas, M. Smith, Q. Jing, U. F. Keyser, J. Cama, S. Kar-Narayan, *Appl. Mater. Today* **2020**, *19*, 100618.
- [33] P. Patil, S. Patil, P. Kate, A. A. Kulkarni, *Nanoscale Adv.* **2021**, *3*, 240.
- [34] E. Gilshstein, S. Bolat, G. T. Sevilla, A. Cabas-Vidani, F. Clemens, T. Graule, A. N. Tiwari, Y. E. Romanyuk, *Adv. Mater. Technol.* **2020**, *5*, 2000369.
- [35] C. Zhang, L. McKeon, M. P. Kremer, S.-H. Park, O. Ronan, A. Seral-Ascaso, S. Barwich, C. Ó. Coileáin, N. McEvoy, H. C. Nerl, B. Anasori, J. N. Coleman, Y. Gogotsi, V. Nicolosi, *Nat. Commun.* **2019**, *10*, 1.
- [36] S. Uzun, M. Schelling, K. Hantanasirisakul, T. S. Mathis, R. Askeland, G. Dion, Y. Gogotsi, *Small* **2020**, *17*, 2006376.
- [37] A. Lee, K. Sudau, K. H. Ahn, S. J. Lee, N. Willenbacher, *Ind. Eng. Chem. Res.* **2012**, *51*, 13195.
- [38] J. F. Salmerón, F. Molina-Lopez, D. Briand, J. J. Ruan, A. Rivadeneyra, M. A. Carvajal, L. F. Capitán-Vallvey, N. F. de Rooij, A. J. Palma, *J. Electron. Mater.* **2013**, *43*, 604.
- [39] M. A. Mohd Asri, N. A. Ramli, A. N. Nordin, *J. Mater. Sci.: Mater. Electron.* **2021**, *32*, 16024.
- [40] D.-J. Lee, D. Y. Kim, *Paper-Based, Hand-Painted Strain Sensor Based on ITO Nanoparticle Channels for Human Motion Monitoring*, Vol. 7, IEEE Access, Manhattan, New York, USA **2019**, pp. 77200–77207.
- [41] T. Lee, Y. W. Choi, G. Lee, P. V. Pikhitsa, D. Kang, S. M. Kim, M. Choi, *J. Mater. Chem. C* **2016**, *4*, 9947.
- [42] S.-H. Park, S.-J. Lee, J. H. Lee, J. Kal, J. Hahn, H.-K. Kim, *Org. Electron.* **2016**, *30*, 112.
- [43] F. Zhu, K. Zhang, E. Guenther, C. S. Jin, *Thin Solid Films* **2000**, *363*, 314.
- [44] P. Jha, S. P. Koiry, V. Saxena, P. Veerender, A. Gusain, A. K. Chauhan, A. K. Debnath, D. K. Aswal, S. K. Gupta, *Org. Electron.* **2013**, *14*, 2635.
- [45] V. Raghuvanshi, D. Bharti, S. P. Tiwari, *Org. Electron.* **2016**, *31*, 177.
- [46] D. Barmpakos, C. Tsamis, G. Kaltsas, *Microelectron. Eng.* **2020**, *225*, 111266.